The initial expansion of the *C. elegans* syncytial germ line is coupled to primordial germ cell cytokinesis incompletion

Jack Bauer[1], Vincent Poupart[1], Eugénie Goupil[1], Ken C. Q. Nguyen[3], David H. Hall[3], and Jean-Claude Labbé[1,2]

[1] Institute for Research in Immunology and Cancer (IRIC), and [2] Department of Pathology and Cell Biology, Université de Montréal, C.P. 6128, Succ. Centre-ville, Montréal, QC, H3C 3J7, Canada.
[3] Department of Neuroscience, Albert Einstein College of Medicine, Bronx, New York 10461, USA

Corresponding author: Jean-Claude Labbé (jc.labbe@umontreal.ca)

Keywords: *C. elegans* germline development, Stable intercellular bridge, Incomplete cytokinesis, Syncytium expansion, Primordial germ cells, Actomyosin.

Summary statement: *C. elegans* germ cells divide within a syncytium in which intercellular bridges are maintained by stable actomyosin rings. We herein demonstrate that stable rings arise *de novo* as a result of incomplete germ cell cytokinesis.

Abstract

The *C. elegans* germline is organized as a syncytium in which each germ cell possesses an intercellular bridge that is maintained by a stable actomyosin ring and that connects it to a common pool of cytoplasm, termed the rachis. How germ cells undergo cytokinesis while maintaining this syncytial architecture is not completely understood. Here we use live imaging to characterize primordial germ cell (PGC) division in *C. elegans* first-stage larvae. We show that each PGC possesses a stable intercellular bridge that connects it to a common pool of cytoplasm, which we term the proto-rachis. We further show that the first PGC cytokinesis is incomplete and that the stabilized cytokinetic ring progressively moves toward the proto-rachis

and eventually integrates into it. Our results support a model in which the initial expansion of the *C. elegans* syncytial germline occurs by incomplete cytokinesis, where one daughter germ cell inherits the actomyosin ring that was newly formed by stabilization of the cytokinetic ring, while the other inherits the pre-existing stable actomyosin ring. We propose that such a mechanism of iterative cytokinesis incompletion underpins *C. elegans* germline expansion and maintenance.

Introduction

The germ line is a specialized tissue that coordinates gamete production and thus ensures fertility in all animal species. Accordingly, primordial germ cell (PGC) specification typically occurs early during embryogenesis to ensure proper distinction from the soma and maintain totipotency (Marlow, 2015; Sybirna et al., 2019). Division of the PGCs will eventually lead to the formation of a pool of germline stem cells that have the capacity to self-renew and give rise to gamete progenitors. One striking feature of certain gamete progenitors, for instance mammalian spermatocytes, Drosophila ovarian cystoblasts and zebrafish germ cells, is the presence of stable intercellular bridges that connect cells with one another, effectively forming a syncytial architecture (Bertho et al., 2021; Fawcett et al., 1959; Greenbaum et al., 2011; Robinson et al., 1994). This feature is common to the germ line of all animals studied to date (Swiatek and Urbisz, 2019), consistent with the notion that intercellular bridges play a fundamental role in fertility. Work in mouse and Drosophila demonstrated that stable germ cell intercellular bridges arise of cytokinetic incompletion at the end of mitosis (Greenbaum et al., 2011; Haglund et al., 2011). While intercellular bridge stabilization was shown to rely on impaired recruitment of the abscission machinery by the protein TEX14 in mouse spermatocytes (Greenbaum et al., 2007; Iwamori et al., 2010) and differential actin regulation at the end of cytokinesis in Drosophila (Robinson et al., 1994; Tilney et al., 1996), our understanding of the molecular mechanism enabling cytokinesis incompletion in animal germ cells remains incomplete.

The adult *C. elegans* germline is contained within two U-shaped gonad arms, in which germ cells form a columnar monolayer around a central core of cytoplasm, termed the rachis (Hall et al., 1999; Hirsh et al., 1976). Except for the germ cells undergoing the last stages of gametogenesis, the entire architecture is syncytial and each cell possesses a stable actomyosin ring that maintains an intercellular bridge (also called ring channel) with the rachis (Amini et al., 2014; Maddox et al., 2005; Priti et al., 2018; Rehain-Bell et al., 2017; Wolke et al., 2007; Zhou et al., 2013). The entire adult germline originates from two PGCs that are born during early

embryogenesis and remain mitotically quiescent until after hatching, when feeding of first-stage larvae (L1) promotes the initiation of their proliferation (Strome and Updike, 2015; Wang and Seydoux, 2013). The cytokinesis leading to PGC formation is incomplete and leaves the two cells connected by a stable intercellular bridge (Goupil et al., 2017), a developmental feature that is common with the division of mouse and Drosophila gamete precursors. Yet, how two PGCs that are directly connected to one another by a single intercellular bridge eventually give rise to thousands of germ cells that each possesses a stable bridge connected to the rachis is not well understood.

Two previous studies, carried out in *C. elegans* and in several species of clitellate annelids, specifically focused on deciphering the mechanism by which germ cells divide within the syncytium (Seidel et al., 2018; Swiatek et al., 2009). Together, these studies suggested a model in which the diameter of the stable intercellular bridge shrinks below the level of optical resolution as a germ cell progresses through mitosis. During mitotic exit, the cytokinetic ring contacts the stable ring at the intercellular bridge, forming a tripartite actomyosin structure, and specific constriction of the cytokinetic ring effectively bisects the intercellular bridge (Seidel et al., 2018; Swiatek et al., 2009). However, the molecular mechanism that would enable the differential regulation of two contacting and intertwined actomyosin rings within the same cell, one dynamic and one stable, is not known. Importantly, neither study employed live imaging of germ cell cytokinesis, which may have masked mechanistically-relevant dynamic events.

Here we use live imaging of the first PGC division to ask how *C. elegans* germ cells undergo cytokinesis to form two daughter cells that each possesses a stable intercellular bridge. We find that each PGC in L1 larvae has an intercellular bridge that opens to a common, adjoining cytoplasmic cavity, which we term the proto-rachis. This indicates that the primordial germ line undergoes a change during late embryogenesis, enabling the formation of at least one additional stable intercellular bridge. We also find that, upon PGC division, the cytokinetic ring persists and integrates into the proto-rachis. Our findings support a model in which PGC cytokinesis is incomplete and ends with an additional stable ring that is inherited by one of the daughter cells, while the other daughter inherits the pre-existing stable actomyosin ring. This mode of incomplete cytokinesis effectively enables expansion of the syncytial architecture when PGCs initiate proliferation, and iteration of this process with each germ cell division could further provide a mechanism for expansion and maintenance of the syncytial architecture throughout development. Our results support the notion that, despite architectural differences between species, cytokinesis incompletion is a fundamental feature of germline development.

Results

Each *C. elegans* PGC possesses a stable intercellular bridge that opens to a common cytoplasmic compartment

The *C. elegans* germ line was previously proposed to be syncytial throughout development (Fig. 1A), however its architecture has not been thoroughly characterized at the L1 stage, where the two primordial germ cells are relatively small and difficult to resolve by light microscopy. To characterize germline organization at the L1 stage, we first performed enhanced-resolution confocal imaging of PGCs co-expressing fluorescent protein (FP)-labelled markers for the plasma membrane (mNeonGreen[mNG]::PH) and chromatin (mCherry[mCh]::HIS-58). As shown previously (Abdu et al., 2016; Lee et al., 2018), we found that the plasma membrane of the two L1-stage PGCs is mostly well resolved except for a region located between the two cells, where a membrane-dense structure, organized into lobes and lacking nuclear material, was present (Fig. 1B). This membrane-dense structure could be observed in all L1 animals examined (n > 100), although its overall size and shape and the number lobes appeared variable. We used transmission electron microscopy (TEM) to validate these observations and gain further insight into this atypical, complex membrane organization. Analysis of serial TEM sections from an individual L1 larva revealed an architecture in which the plasma membrane of the two PGCs appears continuous, with a well-defined intercellular bridge formed between each germ cell and the common, adjoining membrane-dense structure (Fig. 1C-D; Movie 1). Furthermore, while mitochondria could be observed within the cytoplasm of this adjoining membrane-dense structure, including through intercellular bridges (Fig. 1C, inset), no electron-dense signal characteristic of chromatin was detected, consistent with optical microscopy images showing that this structure is devoid of chromatin. These results indicate that each PGC possesses its own distinct intercellular bridge at the L1 larval stage.

Previous findings monitoring the diffusion of photoactivatable rhodamine-dextran indicated that the cytoplasm of PGCs is isolated soon after they are born during embryogenesis but that the two PGCs exchange cytoplasm, and are thus effectively syncytial, after animals have hatched as L1 larvae (Abdu et al., 2016; Amini et al., 2014). To independently validate that PGCs share common cytoplasm at the L1 stage, we employed an approach that made use of animals expressing the photoconvertible fluorescent protein Dendra2 in germ cells (Griffin et al., 2011). To this end, we specifically photoconverted Dendra2 in one of the PGCs, and measured whether the photoconverted signal diffused to the other PGC (Fig. 1E). Our photoconversion method was specific and precise, as the photoconverting laser illumination of one of the PGCs resulted in a rapid peak of fluorescence signal in this cell and no significant measured

fluorescence change in the non-illuminated PGC (Fig. 1F-G; Fig. S1A). Monitoring bleach-corrected photoconverted fluorescence signal intensity over time revealed that it rapidly decreased in the illuminated cell while it concomitantly increased in the other, non-illuminated PGC (Fig. 1F-G; Movie 2). No increase in photoconverted signal was observed in either cell when we imaged animals that had not been illuminated by the photoconverting laser (Fig. S1B), indicating that the photoconverted signal in the non-illuminated PGC originates from the illuminated cell. Consistent with previous findings (Abdu et al., 2016), these results indicate that the intercellular bridges that we observed in the PGCs permit cytoplasmic exchange, and thus that the *C. elegans* primordial germ line is effectively syncytial when animals hatch as L1 larvae.

In *C. elegans* late larvae and adults, each germ cell is connected to the central rachis via an intercellular bridge that is stabilized by an actomyosin ring (Hall et al., 1999; Hirsh et al., 1976; Maddox et al., 2005). In TEM sections, we observed electron-dense regions near the intercellular bridges connecting PGCs to the membrane-dense structure (Fig. 1C-D), suggesting that these bridges may be likewise stabilized by actomyosin rings. To assess this, we used enhanced-resolution confocal microscopy to monitor the localization of several FP-labelled actomyosin regulators previously implicated in the regulation of stable rings at germ cell intercellular bridges in larvae and adults. Their localization was monitored in animals co-expressing fluorescent markers for the plasma membrane, facilitating germ cell identification and characterization. We found that all of the actomyosin regulators that we monitored were generally enriched at the membrane-dense structure located between the PGCs (Fig. 2A; Fig. S2A). Interestingly, several of these regulators, including Non-Muscle Myosin II (NMY-2::GFP) and its regulator CCM-3 (CCM-3::mNG), the Anillin protein ANI-1 (mNG::ANI-1), the *C. elegans*-specific cytokinetic regulator CYK-7 (CYK-7::GFP), and the two centralspindlin complex components CYK-4 (mNG::CYK-4) and ZEN-4 (GFP::ZEN-4), organized into ring-like patterns reminiscent of the actomyosin rings that stabilize the germ cell intercellular bridges in late larvae and adult animals (Fig. 2A; Fig. S2A). To assess this, we measured the fluorescence distribution of membrane and actomyosin markers across PGC intercellular bridges. As reported previously (Amini et al., 2014), stable germ cell intercellular bridges show a distinct pattern of fluorescence distribution for both of these markers in confocal sections: a fluorescence intensity minimum bordered by peaks of fluorescence intensity. We observed this characteristic fluorescence distribution pattern in most (136/154) PGCs of animals expressing FP-tagged ANI-1, NMY-2, CYK-7, CYK-4 and ZEN-4, consistent with the presence of intercellular bridges stabilized by actomyosin rings, as in animals of later developmental stages (Fig. 2B-C; Fig. S2B-E). The measured distance between fluorescence intensity peaks, corresponding to the diameter of the

intercellular bridge, varied from 0.3 to 2 µm (average ± SD = 1.0 ± 0.4 µm, n=136 cells; Fig. 2D). This intercellular bridge diameter is smaller than what was reported for late (L4) larvae and adults (~2-4 µm) but comparable to that measured in L2 and L3 larvae (~1.5 µm; Amini et al., 2014; Rehain-Bell et al., 2017). Well-defined intercellular bridges could not be measured in a small fraction of PGCs analyzed (18/154), which may indicate that some bridges bear a diameter below the limit of optical resolution and/or that their position within the optical plane does not permit proper visualization. These results indicate that, as in other developmental stages, each *C. elegans* PGC intercellular bridge is stabilized by an actomyosin ring.

In addition to accumulating at PGC intercellular bridges, actomyosin regulators could often be observed to form ring-like patterns in other regions of the membrane-dense structure found between the PGCs, specifically near the base of defined membrane lobes (Fig. 2B-C; Fig. S2B-E). Together with points of membrane constriction bordered by electron-dense regions that could be observed by TEM within the membrane-dense structure (Fig. S3A-C; Movie 1), this suggested that membrane lobes are likewise stabilized by actomyosin rings. To assess this, we measured the fluorescence distribution of membrane and actomyosin markers at the base of lobes. Interestingly, we found a fluorescence distribution pattern characteristic of germ cell intercellular bridges (peaks of fluorescence intensities bordering minima), with a bridge diameter comparable to that measured in PGCs and varying between 0.3 and 1.8 µm (average ± SD = 0.7 ± 0.3, n=114 membrane lobes; Fig. 2D). Together, these results indicate that the membrane-dense structure found between the two PGCs at the L1 stage is enriched in contractility regulators that form stable actomyosin rings. These rings stabilize intercellular bridges between the two PGCs and a varying number of membrane lobes and a common, central cavity (Fig. 2E; Movie 3), forming a proto-rachis that bears the same fundamental organization principles as the rachis in adult animals (Fig. 1A).

The PGC cytokinetic ring is stabilized and integrates into the proto-rachis at the end of mitosis

We next sought to exploit the relative simplicity of the germline in L1 larvae to study the mechanism by which germ cell division is coupled to expansion of the syncytial architecture. As each germ cell is connected to the rachis by a stable actomyosin ring from the onset of germline expansion (Fig. 2E), germ cell division must occur through a mechanism that systematically enables the duplication of the stable actomyosin ring. As first step, we imaged populations of developing L1 animals expressing FP-tagged reporters for the plasma membrane and

actomyosin contractility regulators, to characterize the changes in germline architecture that occur when PGCs have undergone their first division. PGCs were previously reported to divide asynchronously (Butuči et al., 2015) and, accordingly, L1 populations contained a significant number of animals with three germ cells, along with those having two (undivided PGCs) and four (both PGCs divided) germ cells (Fig. 3A). We measured the total fluorescence intensity of FP-tagged ANI-1, NMY-2, CYK-7 and CCM-3 at the proto-rachis in gonads comprising two, three and four cells. Except for NMY-2, we found that the fluorescence levels of these actomyosin regulators increased in a unitary step-wise manner as germ cell number increased (Fig. 3A-B). The levels of NMY-2 at the proto-rachis increased significantly between the 2- and 3-germ cell stages but remained stable in 4-germ cell stage larvae (Fig. 3B). These results show that expansion of the proto-rachis during PGC division is tightly coupled to a local increase in actomyosin contractility regulators. As each germ cell possesses an intercellular bridge, this is consistent with the notion that a stable actomyosin ring is added to the proto-rachis with each germ cell division.

To gain further insight into syncytial expansion during germ cell division, we employed live confocal imaging of animals co-expressing FP-tagged ANI-1 and a membrane marker to monitor actomyosin dynamics during PGC division. Because live imaging of PGCs requires that animals are removed from food and germ cells were shown to rapidly exit mitotic proliferation in such conditions (Zellag et al., 2021), we tracked PGC cytokinesis in cells that had already entered mitosis and formed a metaphase plate (Fig. 3C; Movie 4). Analysis of ANI-1 dynamics during PGC cytokinesis revealed two noticeable features. The first one is that the pool of ANI-1 fluorescence in the PGC cytokinetic ring persisted in late cytokinesis and remained visually distinct for at least 20 minutes after the apparent completion of cytokinetic ring ingression (Fig. 3C-D). This contrasts with previous measurements in embryonic blastomeres showing that contractility regulators disappear within ~10 min after the completion of cytokinetic furrow ingression, but is similar to the measured persistence of contractility regulators at the intercellular bridge formed between the two PGCs when they are born (Goupil et al., 2017; Green et al., 2013). The second feature is that the cytokinetic ring ingressed toward the center of the cell and a gap in fluorescence signal could be observed between the pool of ANI-1 at the cytokinetic ring and that at the proto-rachis (Fig. 3C). The presence of such a gap cannot be reconciled with the current model for germ cell division within the syncytium, which proposes that the cytokinetic ring physically contacts the stable actomyosin ring (Seidel et al., 2018; Swiatek et al., 2009). Tracking the gap formed between the pools of ANI-1 at the persistent cytokinetic ring and at the proto-rachis revealed that it progressively decreases (Fig. 3C, E), eventually resulting

in a situation where the two actomyosin pools can no longer be distinguished, suggesting that they have merged. Accordingly, measurements of FP-tagged ANI-1 fluorescence levels at the proto-rachis revealed that they remain relatively stable until late in mitosis, when they increase by an amount that is comparable to that measured in the cytokinetic ring at the end of furrow ingression (Fig. 3F). Similar results were obtained when monitoring NMY-2::GFP dynamics during PGC cytokinesis (Fig. S4; Movie 5). Together with our measured increase in FP-tagged contractility regulators at the proto-rachis with each germ cell division (Fig. 3B), this suggests a model in which abscission is impaired at the end of PGC cytokinesis, resulting in the stabilization of the cytokinetic ring remnant and its integration into the proto-rachis, rather than its transition into a midbody ring and subsequent abscission.

To test this model, we devised an approach enabling us to track more directly the fate of contractility regulators in the cytokinetic ring during PGC division. This was done by specifically photobleaching the mNG::ANI-1 signal present at the proto-rachis in late cytokinesis without impacting the pool of ANI-1 fluorescence in the cytokinetic ring (Fig. 3G-H). We found that the levels of ANI-1 in the cytokinetic ring are relatively stable as mitosis progresses and when this pool progressively integrates that of the proto-rachis (Fig. 3H; Fig. S5C-D). To correct for fluorescence recovery after photobleaching (FRAP) in subsequent timepoints, and thus better assess the contribution of the cytokinetic ring ANI-1 pool to the proto-rachis, we measured the average FRAP of mNG::ANI-1 at the proto-rachis of L1 larvae in which PGCs were not dividing (Fig. S5A-B) and subtracted this amount from the measured mNG::ANI-1 levels at the proto-rachis of larvae undergoing PGC cytokinesis (Fig. S5C-D; see methods). After FRAP correction, we found that the levels of mNG::ANI-1 fluorescence measured at the cytokinetic ring in late mitosis were indistinguishable from those that were measured at the proto-rachis following the integration of the cytokinetic ring signal (Fig. 3H; Fig. S5D). Similar results were obtained when using NMY-2::GFP as actomyosin marker (Fig. S5E-F). These results demonstrate that the pool of actomyosin contractility regulators in the cytokinetic ring directly contributes to the proto-rachis following PGC division. They strongly support a model in which the cytokinetic ring does not undergo its typical maturation prior to abscission, but rather integrates into the proto-rachis as a stable actomyosin ring at the end of cytokinesis, effectively adding one stable ring to the syncytial architecture.

The stable intercellular bridge permits cytoplasmic exchange during PGC cytokinesis

Previous work carried out in adult *C. elegans* animals revealed that the stable actomyosin ring connecting germ cells to the rachis decreases in diameter during germ cell mitosis (Seidel et al., 2018). As PGCs possess a stable actomyosin ring prior to their entry into mitosis, we hypothesized that this stable ring remains open and functional during PGC division and transiently co-exists with the dynamic cytokinetic ring until late cytokinesis, when the two stable rings are each inherited by a daughter cell to maintain their intercellular bridge with the proto-rachis. To test this, we photoconverted Dendra2 in PGCs undergoing cytokinesis (n=12) and measured the dynamics of photoconverted fluorescence levels distribution in illuminated (dividing) and non-illuminated (non-dividing) PGCs. As was observed in mitotically quiescent PGCs (Fig. 1E-G), we found that the photoconverted signal measured in PGCs undergoing cytokinesis progressively decreased and this was concomitant with an increase in photoconverted signal in the other, non-dividing PGCs (Fig. 4A-C; Movie 6). Notably, in all dividing PGCs, fluorescence loss was apparent from the first timepoint after photoconverting illumination and, on average, decreased by 6.6 ± 4.5 % within the first 15 seconds. This is comparable to the decrease of 5.9 ± 4.3% that we measured within the first 15 seconds of photoconversion in mitotically quiescent PGCs (see Fig. 1F). This indicates that dividing PGCs possess an intercellular bridge that allows cytoplasmic exchange with the rest of the primordial germ line and further supports the notion that the pre-existing, stable actomyosin ring present in PGCs prior to their division is maintained as cells progress through mitosis.

Discussion

Together, our work demonstrates that *C. elegans* PGCs are organized as a functional syncytium at the first larval stage and share common cytoplasm through intercellular bridges that are stabilized by actomyosin rings, in an architecture fundamentally similar to that reported for late larvae and adult animals (Fig. 2E; Movie 3). It further shows that the pool of actomyosin contractility regulators in the cytokinetic ring integrates the proto-rachis at the end of mitosis and that the stable intercellular bridge present in PGCs remains open during mitosis. We propose a model in which the initial syncytial expansion of the *C. elegans* germline in L1 larvae occurs by incomplete cytokinesis. In this model, the PGC cytokinetic ring initially forms and ingresses normally but fails to mature into a midbody ring, effectively resulting in a stable actomyosin ring that is specifically inherited by one of the daughter cells, the other germ cell inheriting the pre-existing, stable actomyosin ring (Fig. 5). The molecular mechanism promoting cytokinesis

incompletion is not yet known but may be an integral feature of the *C. elegans* germ line, as birth of the PGCs during embryogenesis was shown to occur by incomplete cytokinesis (Goupil et al., 2017). We thus posit that the incomplete cytokinesis program that is engaged in PGCs during embryogenesis remains active as the germ line expands, enabling the formation of one stable intercellular bridge with each germ cell division. Iterative cytokinesis incompletion was previously demonstrated to sustain germline development in other organisms (Swiatek et al., 2009), most clearly in Drosophila and mouse (Greenbaum et al., 2011; Haglund et al., 2011), suggesting that this mechanism is a conserved feature of germline development in all animals, despite differences in tissue architecture. Furthermore, the notion that daughter germ cells each inherits an "old" (pre-existing) and "new" (cytokinetic) actomyosin ring to maintain intercellular bridges suggests that stable rings are *bona fide* organelles that, like centrioles, undergo controlled duplication during germ cell division.

Our results demonstrate that each PGC in L1 animals possesses an intercellular bridge, an architecture that is strikingly different from that found shortly after PGC birth during embryogenesis, where the two cells are directly connected to one another by a single, stable intercellular bridge (Goupil et al., 2017). This indicates that the syncytial organization of the primordial germ line undergoes significant changes as embryogenesis progresses, enabling the formation of one additional PGC intercellular bridge. One change in primordial germ line organization that was previously documented to take place during embryogenesis is the formation of PGC lobes, which was shown to rely on the formation of actomyosin rings without concomitant mitoses (Abdu et al., 2016; Maniscalco et al., 2020). These extra membranes and actomyosin rings could conceivably be precursor to the proto-rachis that we documented here. However, PGC lobe formation during embryogenesis was demonstrated to occur independently of the centralspindlin components CYK-4 and ZEN-4 (Maniscalco et al., 2020), and we find that both regulators are present at all intercellular bridges of the proto-rachis, whether at a PGC or a membrane lobe. While this raises an apparent discrepancy between PGC lobes formed during embryogenesis and those observed in L1 larvae, we rather favour a hypothesis in which the actomyosin rings that enable PGC lobe formation during embryogenesis eventually mature into *bona fide* intercellular bridges and acquire additional components through this process, such as centralspindlin regulators. They perhaps then serve as a source for the additional PGC bridge that arises in the process.

Finally, our work demonstrates that the two PGCs share cytoplasm during both interphase and cytokinesis, indicating that the stable intercellular bridges remain open throughout cell cycle progression. This is an apparent discrepancy with observations made in adult animals, in which intercellular bridges were shown to drastically decrease in diameter during germ cell mitosis (Seidel et al., 2018). Intercellular bridges were previously shown to be under tension and to demonstrate some degree of lability (Amini et al., 2014; Priti et al., 2018; Rehain-Bell et al., 2017), suggesting that they respond to various forces imparted on the germ line. The closure of stable bridges upon germ cell cytokinesis in adult animals could perhaps be afforded by the capacity to better redistribute forces in this larger rachis, a response that may not be as efficient in a structure as small as the proto-rachis of L1 larvae. Perhaps more puzzling is the notion that the first mitotic entry and division of the two PGCs is asynchronous despite the fact that they share cytoplasm and presumably receive comparable amounts of growth factors. While photoactivatable rhodamine-dextran and Dendra2 can rapidly exchange between cells, diffusion may be more limited for certain cellular components, such as cell cycle and mitotic regulators. In support of this view, the protein DAO-5 was reported to show limited diffusion upon germ cell division in adult animals (Seidel et al., 2018). Whether this is the case for other cellular components will require further investigation.

Materials and Methods

Strains and alleles

The strains and alleles used in this study are listed in Table S1. All strains were maintained at 20°C except for UM785 which was maintained at 25°C, and were grown on nematode growth medium agar plates containing *E. coli* strain OP50, as described previously (Brenner, 1974). First-stage (L1) larvae were obtained by dissolving gravid hermaphrodites in sodium hypochlorite solution (1.2% NaOCl, 250 mM NaOH) and hatching recovered embryos for 24h at room temperature in M9 buffer (22.04 mM KH_2PO_4, 42.27 mM Na_2HPO_4, 85.55 mM NaCl, 1 mM $MgSO_4$). Animals were either processed and imaged as unfed L1 larvae or were imaged after having been transferred to plates with food and grown for 5-7 hours at 25ºC, to allow PGC division.

Confocal microscopy

L1 animals were immobilized in M9 buffer supplemented with 0.2% tetramisole, mounted on a 5% agarose pad and a coverslip was applied and sealed with VaLaP (1:1:1 Vaseline, lanolin, and paraffin). Images were acquired at 16-bit depth with a Zeiss LSM880 laser-scanning confocal microscope, controlled by ZEN black 2.1 SP3 software, and using a Plan-Apochromat 63x/1.4 oil DIC M27 objective.

To acquire enhanced resolution images, a series of 0.2 µm-thick confocal slices comprising the entire primordial germ line were sequentially acquired with 488 nm (argon) and 561 nm (solid state) laser lines and signal was collected by the Zeiss Airyscan detector operated in its super-resolution mode, with a zoom factor of 6 and an optimal frame size of 488 x 488 (except for UM463: 1024 x 1024). Post-acquisition image processing was done with the 2D Airyscan processing tool provided in ZEN black 2.1 SP3.

For time-lapse acquisitions of dividing PGCs, a series of 0.5 µm-thick confocal slices comprising the entire primordial germ line were simultaneously acquired at 2 min intervals with 488 nm and 561 nm laser lines. Signals were respectively collected with a GaAsP and a PMT detector, with a zoom factor of 4, a frame size of 512 x 512 and a frame averaging of 4.

All images were further processed and analyzed using ImageJ software (National Institutes of Health).

Bridge diameter and fluorescence intensity measurements

The diameter of cytoplasmic bridges was determined on single enhanced resolution confocal slices by measuring the fluorescence intensity of FP-tagged membrane and contractility regulators along a 3-pixel-thick line drawn along the membrane of either a PGC or a membrane lobe that faces the proto-rachis (as illustrated in Fig. 2B and Fig. S2B-E). Bridge diameter was determined by measuring the distance between the two maximal peaks of fluorescence for FP-tagged contractility regulators. The fluorescence profile of 18/154 PGCs showed a distance between the two peaks that was less than 0.2 µm or no concomitant decrease in FP-tagged membrane fluorescence, and so these were excluded from the analysis.

The fluorescence intensity of contractility regulators at the proto-rachis and cytokinetic ring were determined by measuring the raw integrated density of a selected region (as depicted in each figure) in sum projections of z-slices comprising the entire primordial germ line. Fluorescence background was measured in the same sum projections, in regions located in the cytoplasm of the PGCs (when possible, otherwise next to the PGCs) and subtracted from

measurements made at the proto-rachis or cytokinetic ring. The cytokinetic ring diameter and the position of the cytokinetic ring midpoint were obtained by measuring the distribution and length of FP-tagged contractility regulator signal along a 1 pixel-wide line drawn along the cytokinetic furrow at each timepoint on sum projections, from furrow initiation until the signal could no more be distinguished from that at the proto-rachis. The center of the proto-rachis was approximated as the center of a circle comprising the entire FP-tagged contractility regulator fluorescence signal at the proto-rachis and was used to measure its distance from the cytokinetic midpoint.

Statistical analyses were done using GraphPad – Prism software.

Fluorescence photobleaching

Samples were mounted as described above, and photobleaching was performed by simultaneously illuminating fluorescence signal at the proto-rachis with 405 nm (solid state) and 454 nm (argon) lasers, both at 100% power and with 100 iterations. Time-lapse images were acquired as described above, at 10 sec intervals for the time points immediately before and after photobleaching, and then at 3 min intervals for the rest of the acquisition.

Contractility regulator fluorescence intensity at the proto-rachis and cytokinetic ring were measured as described above. The rate of fluorescence recovery after photobleaching (FRAP) for FP-tagged contractility regulators was obtained by measuring changes in fluorescence intensity over time at the proto-rachis of L1 larvae in which PGCs were not dividing (Fig. S5A-B). To correct for FRAP, this rate was subtracted at each timepoint from the measured fluorescence intensity at the proto-rachis (Fig. S5C-D).

Dendra2 photoconversion

Samples were mounted as described above, and photoconversion was performed by simultaneously illuminating a selected region in the cytoplasm of a PGC with both 405 nm and 454 nm lasers, at respectively 80% and 20% power and with 500 iterations. For time-lapse acquisitions, a series of 0.8 µm-thick confocal slices comprising the entire primordial germ line were simultaneously acquired at 15 sec intervals with 488 nm and 561 nm laser lines. Signals were respectively collected with a PMT and a GaAsP detector, with a zoom factor of 4, a frame size of 512 x 512 and a frame averaging of 4.

Photoconverted Dendra2 fluorescence intensity was determined by measuring the raw integrated density of a selected region (as depicted in each figure) in sum projections of z-slices comprising the entire primordial germ line, and correcting for photoconverted Dendra2 photobleaching. The rate of photoconverted Dendra2 photobleaching was determined by measuring changes in fluorescence intensity over time in primordial germ lines that had been entirely illuminated by 405 nm and 454 nm laser light (Fig. S1B).

Transmission electron microscopy

Samples were prepared as described in (Hall et al., 2012). Briefly, L1 larvae we fed on bacterial plates for 6 hrs and fixed by high pressure freezing in a Bal-Tec HPM 010 instrument. Samples were then transferred into a primary fix solution of 2% osmium tetroxide and 0.2% uranyl acetate in 98% acetone and 2% dH_2O, and freeze substitution was performed in a Leica EM AFS2 system as follows: -90ºC for 72 hrs, ramp up to -60ºC for 6 hrs (5ºC change per hour), hold at -60ºC for 12 hrs, ramp up to -30ºC (5ºC change per hour), hold at -30ºC for 12 hrs, ramp up to 0ºC for 6 hrs (5ºC change per hour) and hold at 0ºC for another 6 hrs. After 3 washes (20 min each) in pure acetone at 0ºC, samples were washed twice (30 min each) in acetone at room temperature, and transferred to microporous capsules (type C) for embedding. Samples were embedded into Hardplus Embed 812 resin for 2 hrs each in a mix of 1:3 resin/acetone, and 1:1 resin/acetone, then held for 18 hrs in 3:1 resin/acetone, followed by 6 changes in pure resin over 2 days, before curing in a mold at 60ºC for 2 days in an oven. All preparations were then thin sectioned with a thickness of 90 nm using a diamond knife, and serial sections collected on Formvar-coated slot grids. Images were acquired using a FEI Tecnai G2 Spirit BioTwin electron microscope. Images were aligned with the ImageJ TrakEM2 plugin, then nuclei, cells and membrane lobes were colored by manually tracing membranes.

Acknowledgements

We thank Bob Goldstein (UNC Chapel Hill), Erik Griffin (Dartmouth), Amy Maddox (UNC Chapel Hill), Karen Oegema (UC San Diego) and Esther Zanin (LMU Münich) for strains and reagents, and Vincent Archambault, Abigail Gerhold and Greg FitzHarris for comments on the manuscript. We are also grateful to Christian Charbonneau of IRIC's Bio-imaging Facility for technical assistance, Kelly Sears and Jeannie Mui at the McGill University Facility for Electron Microscopy Research for help with microscope operation, and all members of the FitzHarris,

Gerhold, Hickson and Labbé laboratories for helpful discussions. Some strains were provided by the CGC, which is funded by NIH Office of Research Infrastructure Programs (P40 OD010440).

Competing interests

The authors declare no competing interests.

Funding

J. B. received scholarships from IRIC and from Université de Montréal's Graduate Studies and Molecular Biology programs. This study was supported by the National Institutes of Health [grant OD 010943 to D. H. H.] and the Natural Science and Engineering Research Council of Canada [grant RGPIN-2018-04297 to J.-C. L].

Supplemental material

Supplemental material includes 1 table, 5 figures and 6 movies.

References

Abdu, Y., Maniscalco, C., Heddleston, J. M., Chew, T. L. and Nance, J. (2016). Developmentally programmed germ cell remodelling by endodermal cell cannibalism. *Nat Cell Biol* **18**, 1302-1310.

Amini, R., Goupil, E., Labella, S., Zetka, M., Maddox, A. S., Labbé, J. C. and Chartier, N. T. (2014). *C. elegans* Anillin proteins regulate intercellular bridge stability and germline syncytial organization. *J Cell Biol* **206**, 129-143.

Bertho, S., Clapp, M., Banisch, T. U., Bandemer, J., Raz, E. and Marlow, F. L. (2021). Zebrafish *dazl* regulates cystogenesis and germline stem cell specification during the primordial germ cell to germline stem cell transition. *Development* **148**, dev.187773.

Brenner, S. (1974). The genetics of *Caenorhabditis elegans*. *Genetics* **77**, 71-94.

Butuči, M., Williams, A. B., Wong, M. M., Kramer, B. and Michael, W. M. (2015). Zygotic Genome Activation Triggers Chromosome Damage and Checkpoint Signaling in *C. elegans* Primordial Germ Cells. *Dev Cell* **34**, 85-95.

Fawcett, D. W., Ito, S. and Slautterback, D. (1959). The occurrence of intercellular bridges in groups of cells exhibiting synchronous differentiation. *J Biophys Biochem Cytol* **5**, 453-460.

Goupil, E., Amini, R., Hall, D. H. and Labbé, J. C. (2017). Actomyosin contractility regulators stabilize the cytoplasmic bridge between the two primordial germ cells during *Caenorhabditis elegans* embryogenesis. *Mol Biol Cell* **28**, 3789-3800.

Green, R. A., Mayers, J. R., Wang, S., Lewellyn, L., Desai, A., Audhya, A. and Oegema, K. (2013). The midbody ring scaffolds the abscission machinery in the absence of midbody microtubules. *J Cell Biol* **203**, 505-520.

Greenbaum, M. P., Iwamori, T., Buchold, G. M. and Matzuk, M. M. (2011). Germ cell intercellular bridges. *Cold Spring Harb Perspect Biol* **3**, a005850.

Greenbaum, M. P., Ma, L. and Matzuk, M. M. (2007). Conversion of midbodies into germ cell intercellular bridges. *Dev Biol* **305**, 389-396.
Griffin, E. E., Odde, D. J. and Seydoux, G. (2011). Regulation of the MEX-5 gradient by a spatially segregated kinase/phosphatase cycle. *Cell* **146**, 955-968.
Haglund, K., Nezis, I. P. and Stenmark, H. (2011). Structure and functions of stable intercellular bridges formed by incomplete cytokinesis during development. *Commun Integr Biol* **4**, 1-9.
Hall, D. H., Winfrey, V. P., Blaeuer, G., Hoffman, L. H., Furuta, T., Rose, K. L., Hobert, O. and Greenstein, D. (1999). Ultrastructural features of the adult hermaphrodite gonad of *Caenorhabditis elegans*: relations between the germ line and soma. *Dev Biol* **212**, 101-123.
Hirsh, D., Oppenheim, D. and Klass, M. (1976). Development of the reproductive system of *Caenorhabditis elegans*. *Dev Biol* **49**, 200-219.
Iwamori, T., Iwamori, N., Ma, L., Edson, M. A., Greenbaum, M. P. and Matzuk, M. M. (2010). TEX14 interacts with CEP55 to block cell abscission. *Mol Cell Biol* **30**, 2280-2292.
Lee, K. Y., Green, R. A., Gutierrez, E., Gomez-Cavazos, J. S., Kolotuev, I., Wang, S., Desai, A., Groisman, A. and Oegema, K. (2018). CYK-4 functions independently of its centralspindlin partner ZEN-4 to cellularize oocytes in germline syncytia. *Elife* **7**.
Maddox, A. S., Habermann, B., Desai, A. and Oegema, K. (2005). Distinct roles for two *C. elegans* anillins in the gonad and early embryo. *Development* **132**, 2837-2848.
Maniscalco, C., Hall, A. E. and Nance, J. (2020). An interphase contractile ring reshapes primordial germ cells to allow bulk cytoplasmic remodeling. *J Cell Biol* **219**.
Marlow, F. (2015). Primordial Germ Cell Specification and Migration. *F1000Res* **4**.
Priti, A., Ong, H. T., Toyama, Y., Padmanabhan, A., Dasgupta, S., Krajnc, M. and Zaidel-Bar, R. (2018). Syncytial germline architecture is actively maintained by contraction of an internal actomyosin corset. *Nat Commun* **9**, 4694.
Rehain-Bell, K., Love, A., Werner, M. E., MacLeod, I., Yates, J. R., 3rd and Maddox, A. S. (2017). A Sterile 20 Family Kinase and Its Co-factor CCM-3 Regulate Contractile Ring Proteins on Germline Intercellular Bridges. *Curr Biol* **27**, 860-867.
Robinson, D. N., Cant, K. and Cooley, L. (1994). Morphogenesis of Drosophila ovarian ring canals. *Development* **120**, 2015-2025.
Seidel, H. S., Smith, T. A., Evans, J. K., Stamper, J. Q., Mast, T. G. and Kimble, J. (2018). *C. elegans* germ cells divide and differentiate in a folded tissue. *Dev Biol* **442**, 173-187.
Strome, S. and Updike, D. (2015). Specifying and protecting germ cell fate. *Nat Rev Mol Cell Biol* **16**, 406-416.
Swiatek, P., Kubrakiewicz, J. and Klag, J. (2009). Formation of germ-line cysts with a central cytoplasmic core is accompanied by specific orientation of mitotic spindles and partitioning of existing intercellular bridges. *Cell Tissue Res* **337**, 137-148.
Swiatek, P. and Urbisz, A. Z. (2019). Architecture and Life History of Female Germ-Line Cysts in Clitellate Annelids. *Results Probl Cell Differ* **68**, 515-551.
Sybirna, A., Wong, F. C. K. and Surani, M. A. (2019). Genetic basis for primordial germ cells specification in mouse and human: Conserved and divergent roles of PRDM and SOX transcription factors. *Curr Top Dev Biol* **135**, 35-89.
Tilney, L. G., Tilney, M. S. and Guild, G. M. (1996). Formation of actin filament bundles in the ring canals of developing Drosophila follicles. *J Cell Biol* **133**, 61-74.
Wang, J. T. and Seydoux, G. (2013). Germ cell specification. *Advances in experimental medicine and biology* **757**, 17-39.
Wolke, U., Jezuit, E. A. and Priess, J. R. (2007). Actin-dependent cytoplasmic streaming in *C. elegans* oogenesis. *Development* **134**, 2227-2236.

Zellag, R. M., Zhao, Y., Poupart, V., Singh, R., Labbé, J. C. and Gerhold, A. R. (2021). CentTracker: a trainable, machine learning-based tool for large-scale analyses of *C. elegans* germline stem cell mitosis. *Mol Biol Cell* **32**, 915-930.

Zhou, K., Rolls, M. M. and Hanna-Rose, W. (2013). A postmitotic function and distinct localization mechanism for centralspindlin at a stable intercellular bridge. *Dev Biol* **376**, 13-22.

Figures

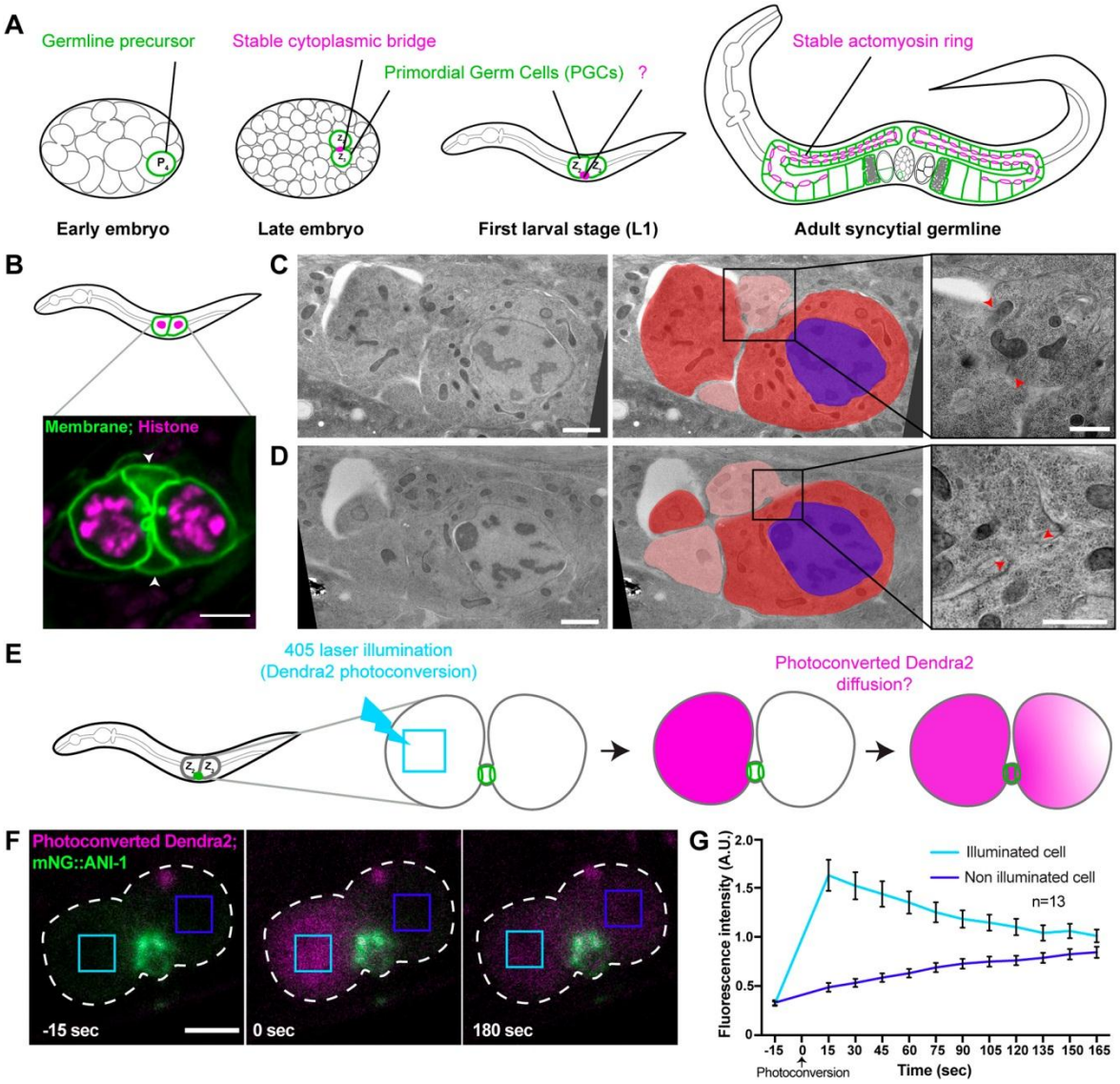

Figure 1. Both PGCs have an intercellular bridge in *C. elegans* first-stage larvae. (A) Schematic representation of stages of *C. elegans* germline development, from birth of the two PGCs (Z_2 and Z_3) following division of the germ cell precursor P_4 during embryogenesis to the adult architecture. Germ cell plasma membrane is in green and actomyosin rings stabilizing intercellular bridges are in magenta. (B) Confocal images (sum projection of 3 slices) of the PGCs in a first larval stage animal expressing markers for membrane (mNG-PH$^{PLC\delta}$, green) and chromatin (mCh-HIS-58, magenta). White arrowheads point to the membrane-dense structure found between the two PGCs. Scale bar = 3 µm. (C, D) Selected transmission electron

microscopy images from 90 nm-thick sections of the primordial germ line from a first larval stage animal. The middle panel is a color-overlayed version of the left panel, depicting nuclei (blue), PGC cytoplasm (dark red) and cytoplasm within the membrane-dense structure between the PGCs (light red). Scale bar = 1 µm. Insets on the right are magnifications of the boxed regions in the middle panels, where intercellular bridges are visible (red arrowheads). Scale bar = 500 nm. (E) Schematic representation of the Dendra2 photoconversion and diffusion approach to assess cytoplasmic exchange in first larval stage PGCs. (F) Confocal time-lapse images (sum projection of 3 slices) of PGCs in animals expressing mNG::ANI-1 (green) and Dendra2 before (left) and after (middle & right) Dendra2 photoconversion (magenta). The blue boxes indicate regions where fluorescence was measured over time, and the light blue box in the middle panel is where photoconverting laser illumination was done. Scale bar = 3 µm. (G) Mean levels of photoconverted Dendra2 fluorescence intensity measured over time (in seconds) in the illuminated (light blue) and non-illuminated (dark blue) regions of the PGCs that are defined in (F). Time 0 is the onset of photoconverting laser illumination. Error bars are standard error of the mean, n = 13 animals.

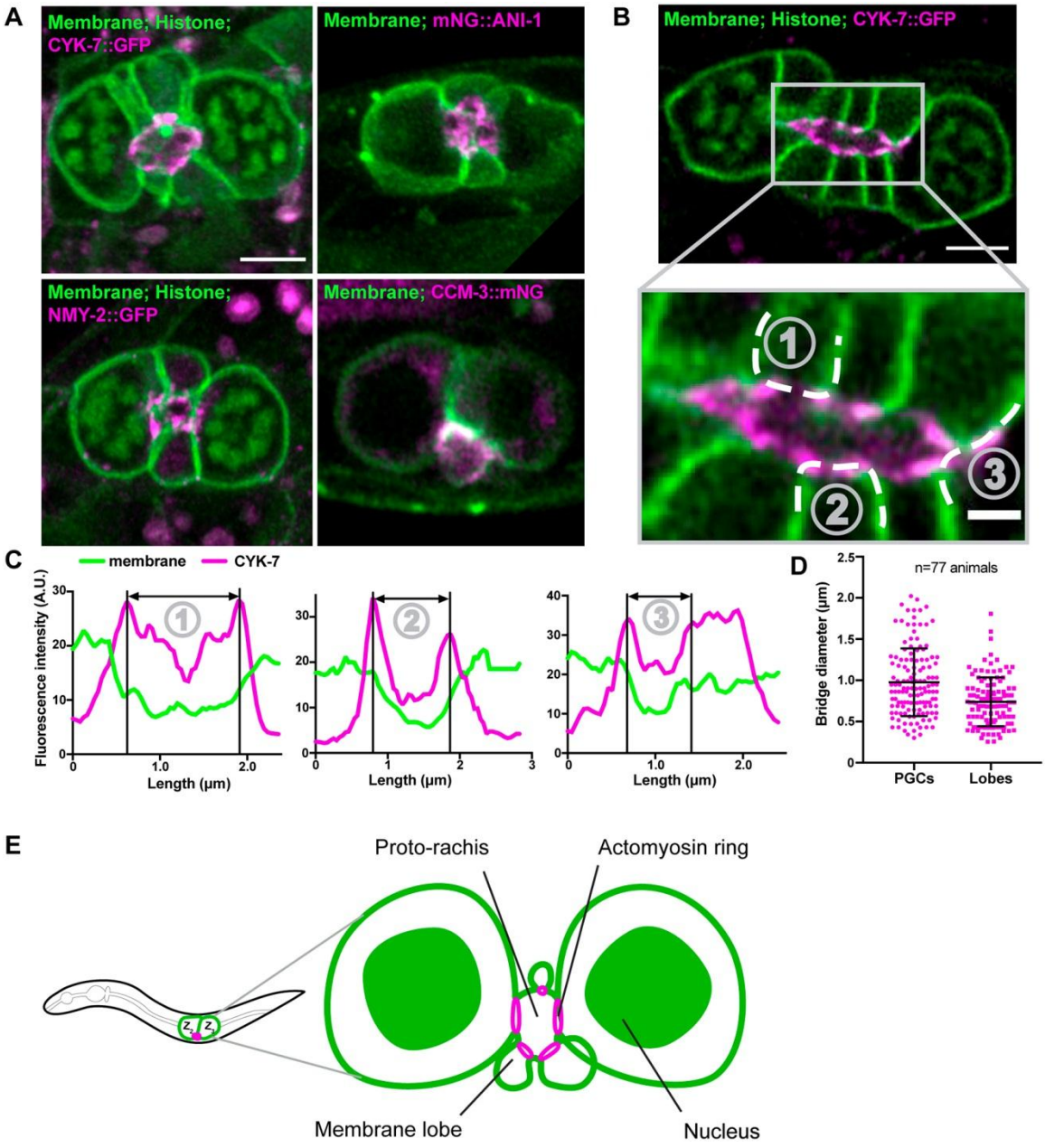

Figure 2. Actomyosin rings organize a functional proto-rachis in the *C. elegans* primordial germ line. (A) Confocal images (maximum projection of 3 slices) of the PGCs in first larval stage animals expressing FP-tagged markers for membrane and chromatin (TagRFP-PH$^{PLC\delta}$ & mCh-HIS-58, green) and specified actomyosin contractility regulators (magenta). Scale bar = 3 µm. (B) Same as in (A) but for a single confocal slice instead of a maximum projection. The inset depicts cortical regions in lobes (1 & 2) and a PGC (3) where fluorescence intensity was measured. Scale bars = 3 µm (top) and 1 µm (inset, bottom). (C) Fluorescence intensity of membrane (TagRFP-PH$^{PLC\delta}$, green) or CYK-7::GFP (magenta) signal measured along each line

(1-3) drawn in the inset of (B). Intensity peaks of CYK-7::GFP define bridge diameter (black lines and arrows). (D) Intercellular bridge diameters (in µm) measured in PGCs (n = 136) or lobes (n = 114) of animals co-expressing a membrane marker and either CYK-7::GFP, mNG::ANI-1, NMY-2::GFP, mNG::CYK-4 or GFP::ZEN-4 (n = 77 animals in total). Lines represent mean ± standard deviation. (E) Schematic representation of the *C. elegans* primordial germ line at the first larval stage. Each PGC has an actomyosin ring that stabilizes an intercellular bridge open to a central proto-rachis. The proto-rachis bears a varying number of membrane lobes (3 are depicted here) that are also defined by actomyosin rings.

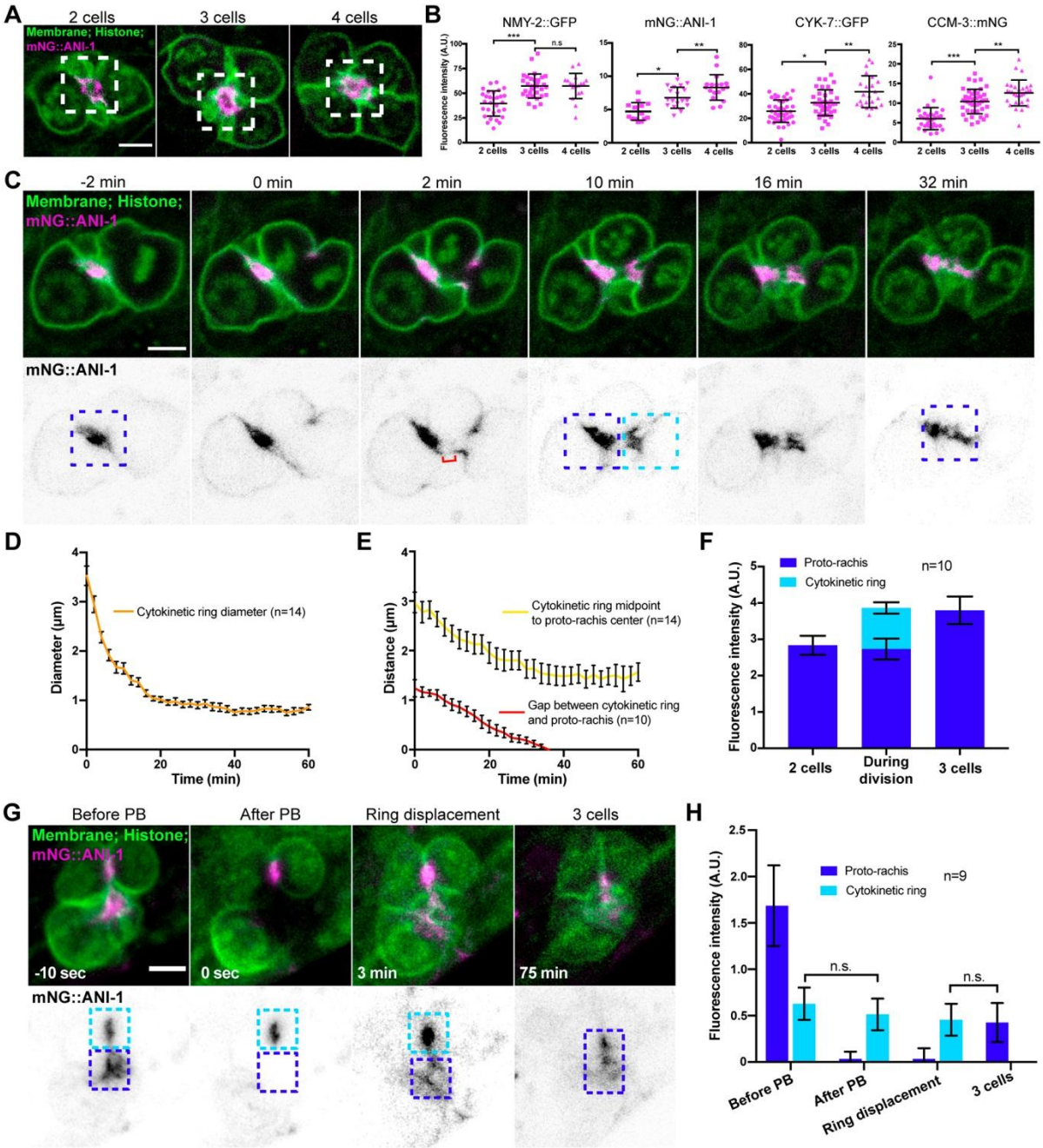

Figure 3. The cytokinetic ring integrates and expands the proto-rachis at the end of PGC division. (A) Confocal images (maximum projection of 3 slices) of the primordial germ line containing 2 (left), 3 (middle) and 4 (right) germ cells in first larval stage animals co-expressing markers for membrane and chromatin (TagRFP-PH$^{PLC\delta}$ & mCh-HIS-58, green) and mNG::ANI-1 (magenta). Dashed boxes indicate regions where fluorescence intensity was measured. (B) Measured sum fluorescence intensity of the specified markers of actomyosin contractility at the proto-rachis of first larval stage animals possessing 2, 3 and 4 germ cells. Lines represent

median ± standard deviation. Statistical analyses were done using a one-way ANOVA test with a Tukey *post hoc* test (* = $p < 0.03$; ** = $p < 0.01$; **** = $p < 0.0001$). (C) Confocal time-lapse images (sum projection of 3 slices) of PGCs undergoing first division in animals co-expressing markers for membrane and chromatin (TagRFP-PH$^{PLC\delta}$ & mCh-HIS-58, green) and mNG::ANI-1 (magenta & bottom panels). The boxes indicate regions where fluorescence intensity was measured at the cytokinetic ring (light blue) and proto-rachis (dark blue) at the specified stages of cytokinesis. The bracket (red) indicates the gap between the cytokinetic ring and the proto-rachis. Time 0 is the onset of cytokinetic ring ingression. (D-E) Measures of cytokinetic ring diameter (D; n = 14) and distance between the cytokinetic ring midpoint and the center of the proto-rachis (yellow line; n = 14) or the gap between the cytokinetic ring and the proto-rachis (red line; n = 10; E) over time in animals imaged as in (C). Error bars represent standard error of the mean. (F) Mean levels of mNG::ANI-1 sum fluorescence intensity measured at the proto-rachis (dark blue) and cytokinetic ring (light blue, as depicted in C) before (2 cells), during and after (3 cells) PGC division. Error bars represent standard error of the mean, n = 10. (G) Confocal time-lapse images (sum projection of 3 slices) of PGCs undergoing first division in animals co-expressing markers for membrane and chromatin (TagRFP-PH$^{PLC\delta}$ & mCh-HIS-58, green) and mNG::ANI-1 (magenta & bottom panels), taken before and after photobleaching (PB) of the signal at the proto-rachis (time 0). The boxes indicate regions where fluorescence intensity was measured at the cytokinetic ring (light blue) and proto-rachis (dark blue) over time. (H) Mean bleach-corrected levels of mNG::ANI-1 sum fluorescence intensity measured at the proto-rachis (dark blue) and cytokinetic ring (light blue, as depicted in G) before and after photobleaching (PB) of the signal at the proto-rachis. Error bars are standard error of the mean, n = 9 animals. Statistical analyses were done using a one-way ANOVA test with a Tukey *post hoc* test (ns = not significant, $p > 0.92$). In all panels, scale bar = 3 µm.

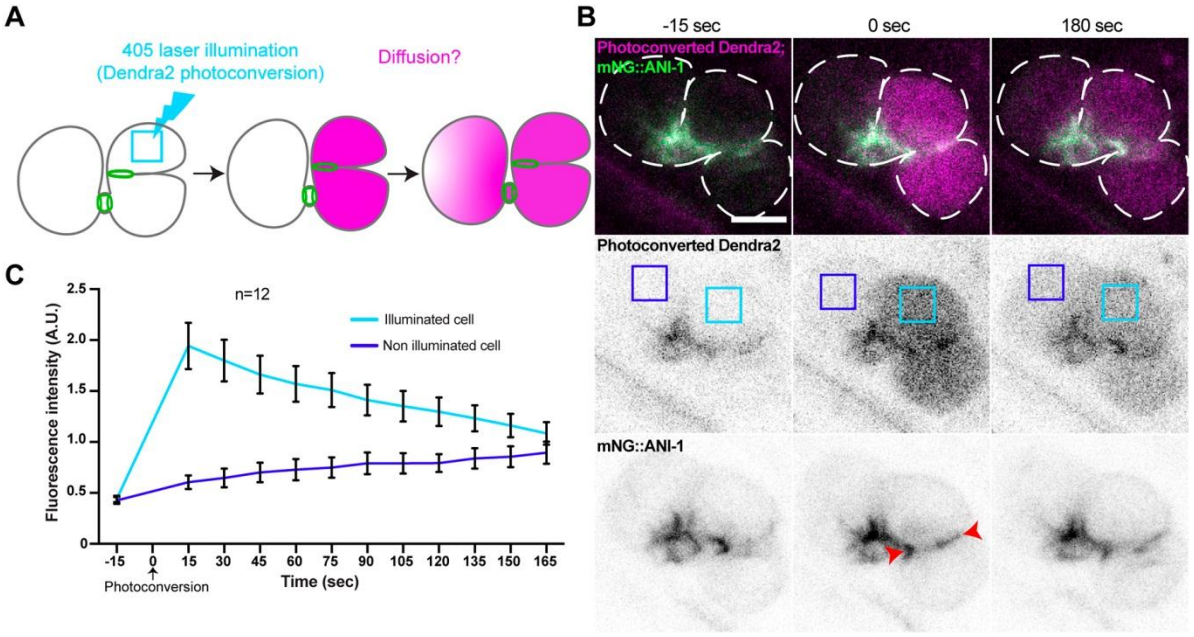

Figure 4. PGCs maintain their intercellular bridge to the proto-rachis during division. (A) Schematic representation of the Dendra2 photoconversion and diffusion approach to assess cytoplasmic exchange in a dividing PGC. (B) Confocal time-lapse images (sum projection of 3 slices) of PGCs in animals expressing mNG::ANI-1 (green) and Dendra2 before (left) and after (middle & right) Dendra2 photoconversion (magenta). The blue boxes in the middle panel indicate regions where fluorescence was measured over time, and the light blue box in the center panel is where photoconverting laser illumination was done. Red arrowheads in the bottom panel delineate the cytokinetic ring. Scale bar = 3 μm. (C) Mean levels of photoconverted Dendra2 fluorescence intensity measured over time (in seconds) in the illuminated (light blue) and non-illuminated (dark blue) regions of the PGCs that are defined in (B). Time 0 is the onset of photoconverting laser illumination. Error bars are standard error of the mean, n = 12 animals.

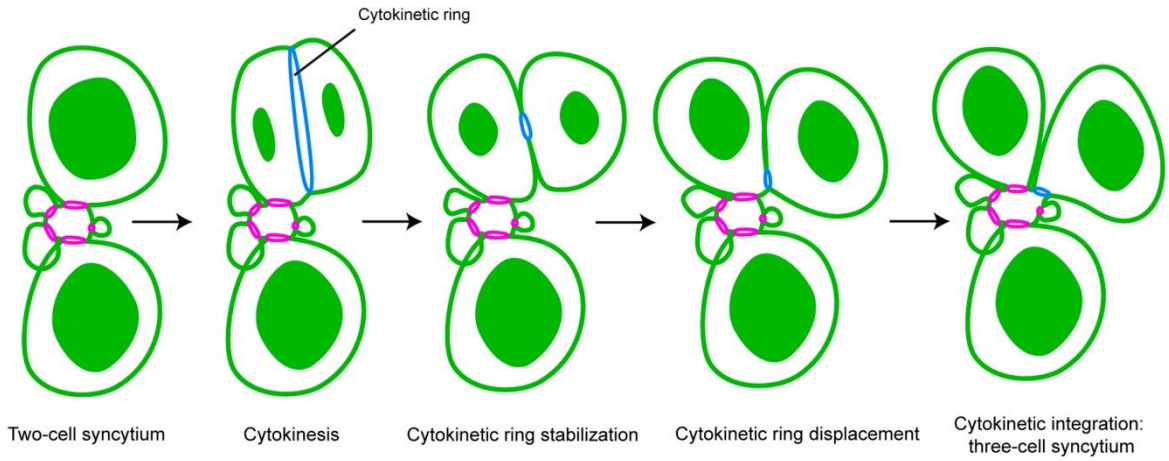

Figure 5. Proposed model for initial expansion of the primordial *C. elegans* germ line by incomplete PGC cytokinesis. The model depicts plasma membrane and chromatin in green, stable intercellular bridges in magenta and the cytokinetic ring in blue at various mitotic stages. See main text for details.

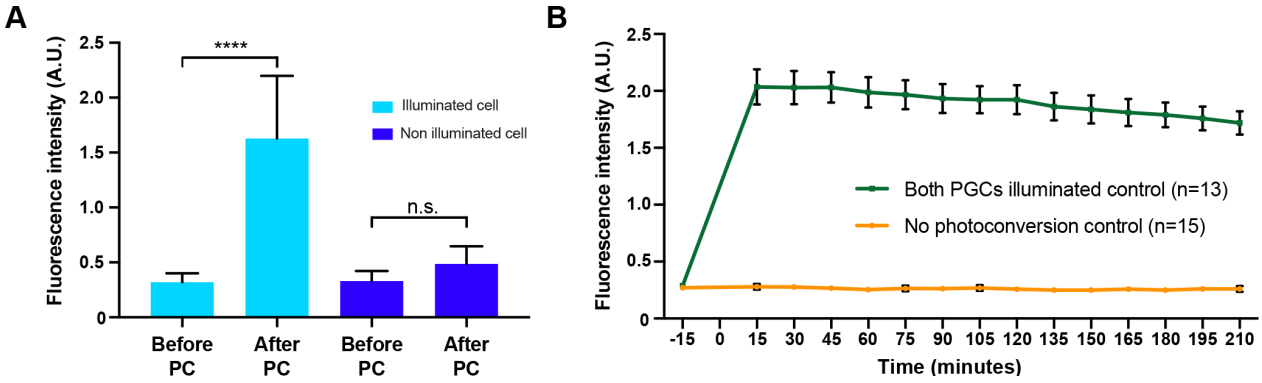

Fig. S1. (A) Mean levels of photoconverted Dendra2 fluorescence intensity measured before and immediately after photoconversion (PC) in the illuminated (light blue) and non-illuminated (dark blue) regions of the PGCs that are defined in Figure 1F. Dendra2 photoconversion in one cell (light blue) does not significantly impact fluorescence levels in the other cell (dark blue). Error bars are standard error of the mean, n = 13 animals. Statistical analyses were done using a one-way ANOVA test with a Tukey *post hoc* test (ns = not significant, p = 0.55, **** = p < 0.0001). (B) Mean levels of photoconverted Dendra2 fluorescence intensity measured over time (in seconds) when the entire primordial germ line is illuminated by the photoconverting laser at time 0 (green line, n = 15) or when no photoconverting laser illumination is performed (orange line, n = 13). Error bars are standard error of the mean.

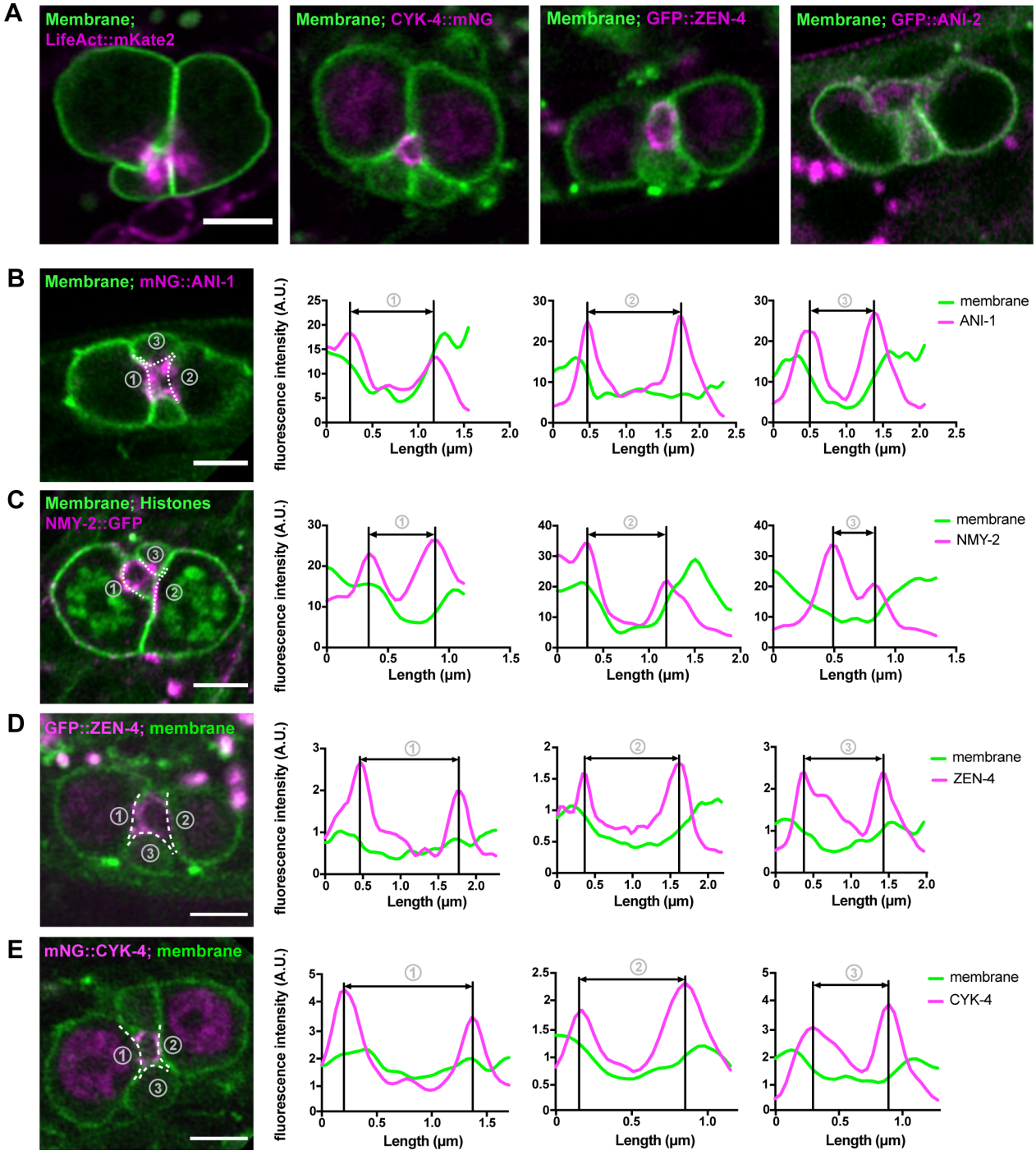

Fig. S2. (A) Confocal images (sum projection of 3 slices) of the PGCs in first larval stage animals expressing FP-tagged markers for membrane (mCh-PH$^{PLC\delta}$ or GFP-PH$^{PLC\delta}$, green) and specified actomyosin contractility regulators (magenta). (B-E) Same as in (C) but for a single confocal slice instead of a sum projection for animals expressing mNG::ANI-1 (B), NMY-2::GFP (C), GFP::ZEN-4 (D) and mNG::CYK-4 (E). The three graphs on the right report the fluorescence intensity of membrane (green) or contractility regulator (magenta) signal measured along each dotted line (1-3) drawn in the image on the left. Intensity peaks of contractility regulators define bridge diameter (black lines and arrows). In all panels, scale bar = 3μm.

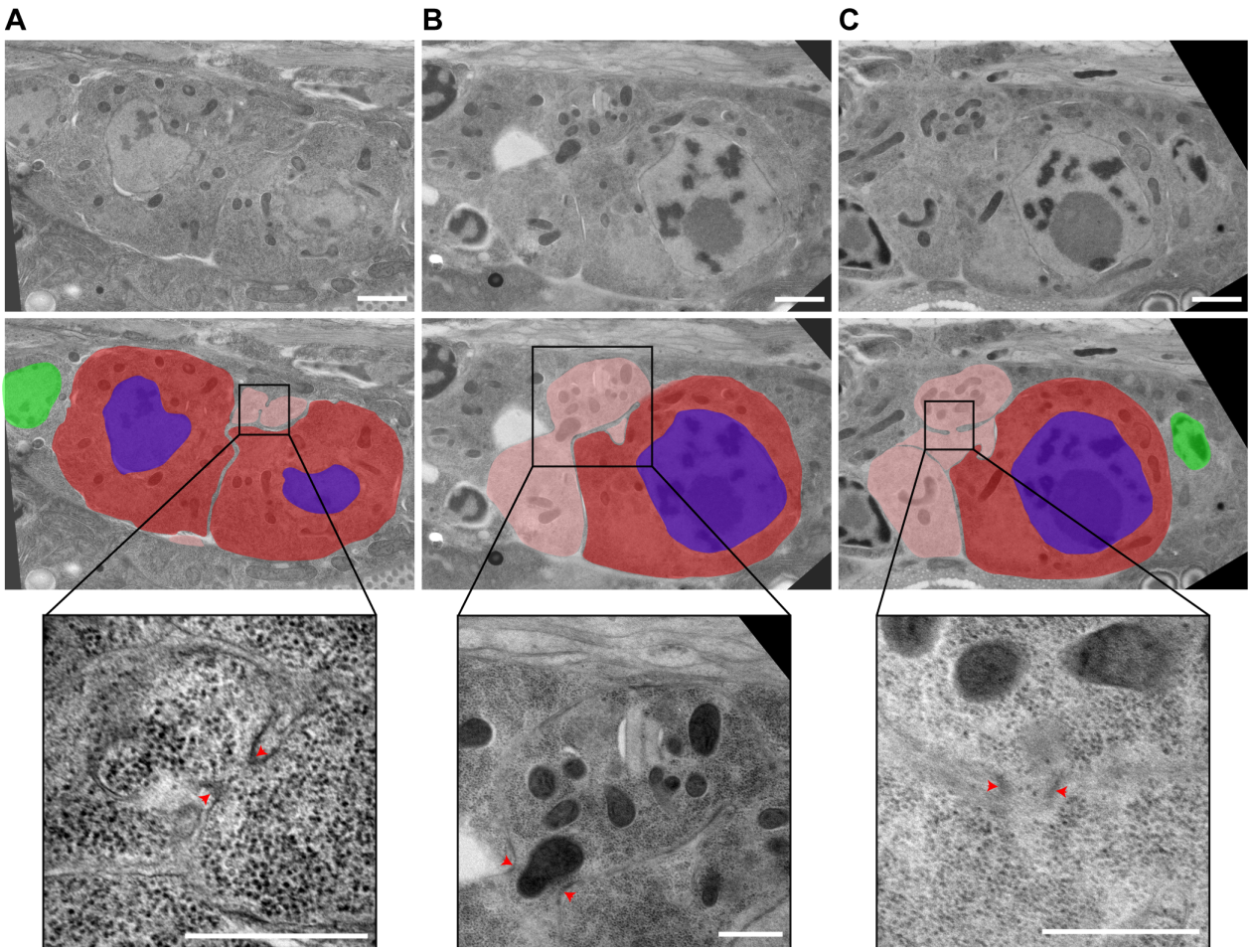

Fig. S3. (A-C) Selected TEM images from 90 nm-thick sections of the primordial germ line from a first larval stage animal. The middle panel is a color-overlayed version of the top panel, depicting nuclei (blue), PGC cytoplasm (dark red) and cytoplasm within the membrane-dense structure between the PGCs (light red). Scale bar = 1 µm. Insets at the bottom are magnifications of the boxed regions in the middle panels, where cytoplasmic bridges are visible within the membrane-dense structure (red arrowheads), possibly at the base of membrane lobes. The nuclei of the somatic primordial gonad (Z_1 and Z_4) are depicted in green. Scale bar = 500 nm.

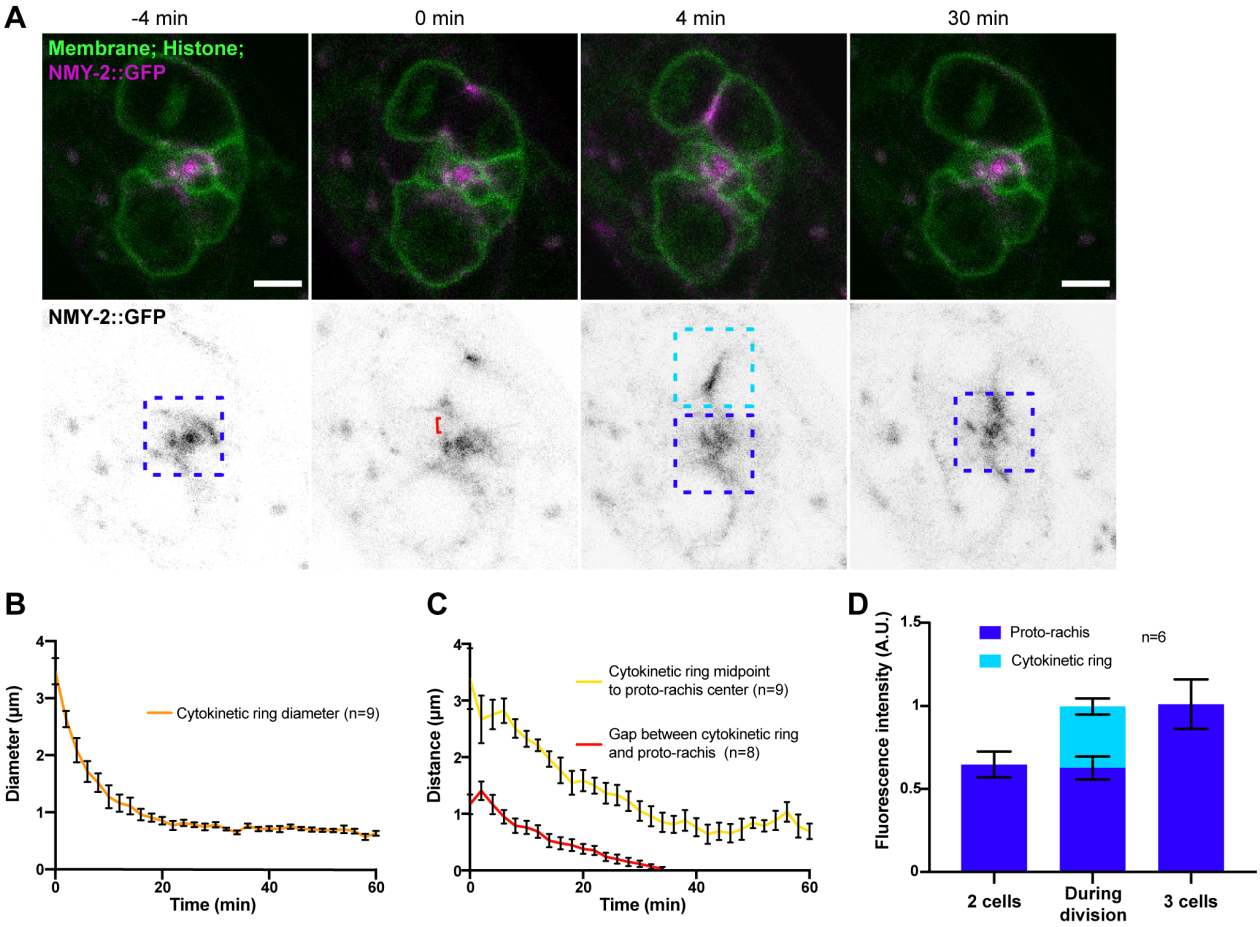

Fig. S4. (A) Confocal time-lapse images (sum projection of 3 slices) of PGCs undergoing first division in animals co-expressing markers for membrane and chromatin (TagRFP-PH$^{PLC\delta}$ & mCh-HIS-58, green) and NMY-2::GFP (magenta & bottom panels). The boxes indicate regions where fluorescence intensity was measured at the cytokinetic ring (light blue) and proto-rachis (dark blue) at the specified stages of cytokinesis. The bracket (red) indicates the gap between the cytokinetic ring and the proto-rachis. Time 0 is the onset of cytokinetic ring ingression. Scale bar = 3µm. (B-C) Measures of cytokinetic ring diameter (B; n = 9) and distance between the cytokinetic ring midpoint and the center of the proto-rachis (yellow line; n = 9) or the gap between the cytokinetic ring and the proto-rachis (red line; n = 8; C) over time in animals imaged as in (A). Error bars represent standard error of the mean. (D) Mean levels of NMY-2::GFP sum fluorescence intensity measured at the proto-rachis (dark blue) and cytokinetic ring (light blue, as depicted in A) before (2 cells), during and after (3 cells) PGC division. Error bars represent standard error of the mean, n = 6.

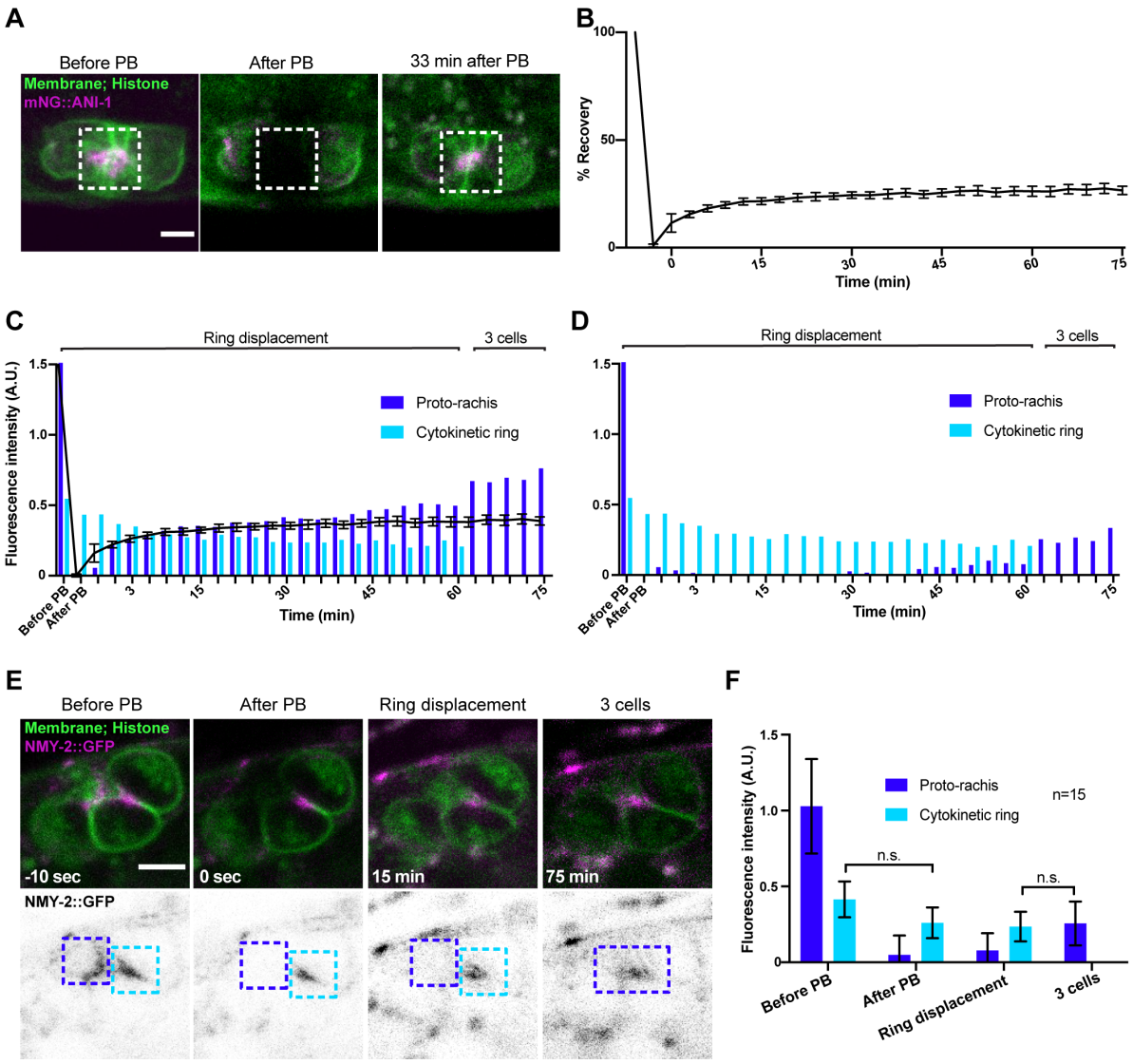

Fig. S5. (A) Confocal time-lapse images (sum projection of 3 slices) of non-dividing (mitotically quiescent) PGCs in animals co-expressing markers for membrane and chromatin (TagRFP-PH$^{PLC\delta}$ & mCh-HIS-58, green) and mNG::ANI-1 (magenta), taken before and after photobleaching (PB) of the signal at the proto-rachis (time 0). The boxes indicate regions where fluorescence intensity was measured at the proto-rachis over time. (B) Mean percentage of mNG::ANI-1 fluorescence recovery after photobleaching (FRAP) measured at the proto-rachis (as depicted in A). Error bars are standard error of the mean, n = 8 animals. (C-D) Mean levels of mNG::ANI-1 sum fluorescence intensity measured at the proto-rachis (dark blue) and cytokinetic ring (light blue, as depicted in Figure 3G) before and after photobleaching (PB) of the signal at the proto-rachis. The percent mNG::ANI-1 FRAP measured in B is overlayed in panel C and panel D represents the values at each timepoint after subtraction of these relative FRAP levels are subtracted from the measured fluorescence levels at the proto-rachis, thus effectively correcting for FRAP. (E) Confocal time-lapse images (sum projection of 3 slices) of PGCs undergoing first division in animals co-expressing markers for membrane and chromatin (TagRFP-PH$^{PLC\delta}$ & mCh-HIS-58, green) and NMY-2::GFP (magenta & bottom panels), taken before and after photobleaching (PB) of the signal at the proto-rachis (time 0). The boxes indicate regions where fluorescence intensity was measured at the cytokinetic ring (light blue) and proto-rachis (dark blue) over time. (F) Mean bleach-corrected levels of GFP::NMY-2 sum fluorescence intensity measured at the proto-rachis (dark blue) and cytokinetic ring (light blue, as depicted in E) before and after photobleaching (PB) of the signal at the proto-rachis. Error bars are standard error of the mean, n = 15 animals. Statistical analyses were done using an ordinary one-way ANOVA test with a Tukey post hoc test (ns = not significant, $p > 0.12$). In all panels, scale bar = 3μm.

Table S1. Strains used in this study

Strain	Genotype	Allele Reference
N2	Wild type	2
UM208	*unc-119(ed3) III; ltIs81[Ppie-1::gfp-tev-Stag::ani-2; unc-119(+)]; ltIs44[Ppie-1::mCherry::PH(PLC1delta1); unc-119(+)]*	1, 8
UM463	*cpIs42[Pmex-5::mNeonGreen::PLCδ-PH::tbb-2 3'UTR; unc-119(+)] II; ltIs37[pAA64; Ppie-1::mCherry::HIS-58; unc-119(+)] IV*	7, 11
UM639	*cpSi20[Pmex-5::TAGRFPT::PH::tbb-2 3'UTR; unc-119(+)] II; zuIs45[Pnmy-2::nmy-2::GFP; unc-119(+)]; ltIs37 [pAA64; Ppie-1::mCherry::HIS-58; unc-119(+)] IV*	7, 11, 12
UM641	*cpSi20[Pmex-5::TAGRFPT::PH::tbb-2 3'UTR; unc-119 (+)] II; ani-1(mon7[mNeonGreen^3xFlag::ani-1]) III; unc-119 (ed3) III*	7, 13
UM655	*cpSi20[Pmex-5::TAGRFPT::PH::tbb-2 3'UTR; unc-119 (+)] II; ani-1(mon7[mNeonGreen^3xFlag::ani-1]) III; unc-119(ed3)* III; ltIs37 [pAA64; Ppie-1::mCherry::HIS-58; unc-119(+)] IV*	7, 11, 13
UM717	*cp52[nmy-2::mkate2 + LoxP unc-119(+) LoxP] I; ccm-3(mon9[ccm-3::mNeonGreen^3xFlag]) II; unc-119(ed3)* III; ltIs44[pAA173, Ppie-1::mCherry::PH(PLC1delta1); unc-119(+)]*	4, 8, 13
UM735	*xnSi1[Pmex-5::GFP::PH(PLC1delta1)::nos-2 3'UTR] II; estSi71[pAC257;Pmex-5::lifeAct::mKate2::tbb-2 3'UTR; cb-unc-119(+)] IV*	3, 10
UM740	*cpSi20[Pmex-5::TAGRFPT::PH::tbb-2 3'UTR; unc-119 (+)] II; ltIs37 [pAA64; Ppie-1::mCherry::HIS-58; unc-119(+)] IV; ltIs154 [pOD539(pBG3); Ppie-1::cyk-7::GFP; unc-119 (+)]*	5, 7, 11
UM785	*axIs1959[Ppie-1::Dendra2::TEV::S-peptide::pie-1 3'UTR; unc-119(+)]; ani-1(mon7[mNeonGreen^3xFlag::ani-1]) III; unc-119(ed3)* III; ojIs1[Ppie-1::GFP::tbb-2; unc-119(+)] V*	6, 13, 14
OD3840	*ltSi849[pKL120; Pmex-5::mCherry::PH(PLC1delta1)::tbb-2 3'UTR; cb-unc-119(+)] I; unc-119(ed3)* III; zen-4(lt30[GFP::loxP::zen-4]) IV*	9
OD3686	*ltSi849[pKL120; Pmex-5::mCherry::PH(PLC1delta1)::tbb-2 3'UTR; cb-unc-119(+)] I; ltSi1124[pSG092; Pcyk-4::CYK- 4reencoded::mNeonGreen::cyk-4 3'-UTR; cb- unc-119(+)] II; unc- 119(ed3) III*	9

* *unc-119(ed3)* was in the parental strain but may not be present in this strain.

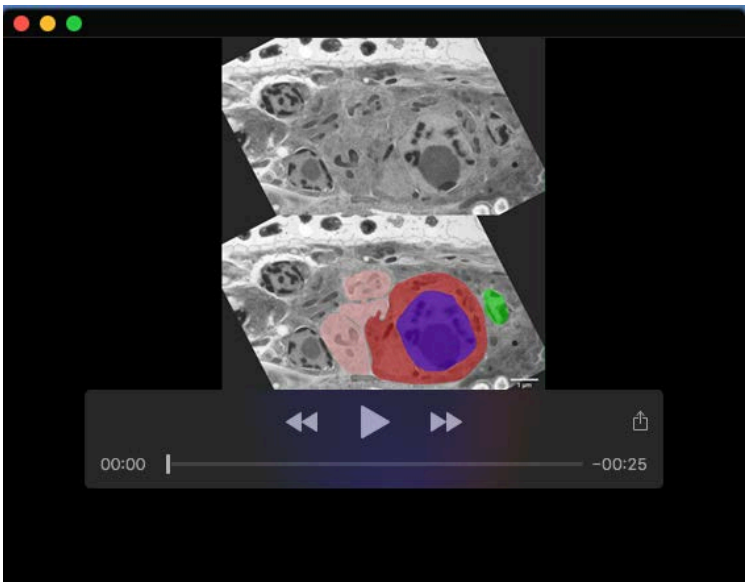

Movie 1. Serial transmission electron microscopy images from 90 nm-thick sections of the primordial germ line from a first larval stage animal. The bottom panel is a color-overlayed version of the top panel, depicting nuclei (blue), PGC cytoplasm (dark red) and cytoplasm within the membrane-dense structure between the PGCs (i.e. the proto-rachis, light red). The nuclei of the somatic primordial gonad (Z_1 and Z_4) are depicted in green. Images were aligned manually.

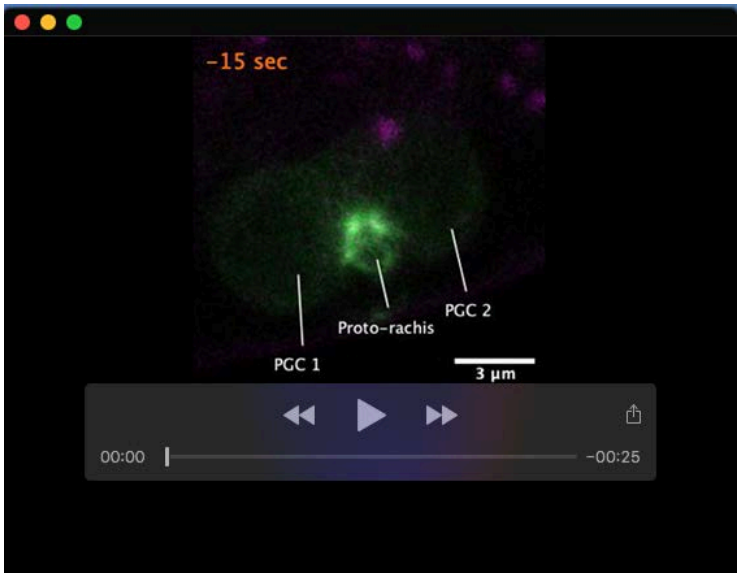

Movie 2. Time-lapse movie of the primordial germ line with two mitotically quiescent PGCs before and after Dendra2 fluorescence photoconversion (same images as shown in figure 1F), in animals co-expressing mNG::ANI-1 and cytoplasmic Dendra2. Images were acquired every 15 sec and are played at 1 frame per sec.

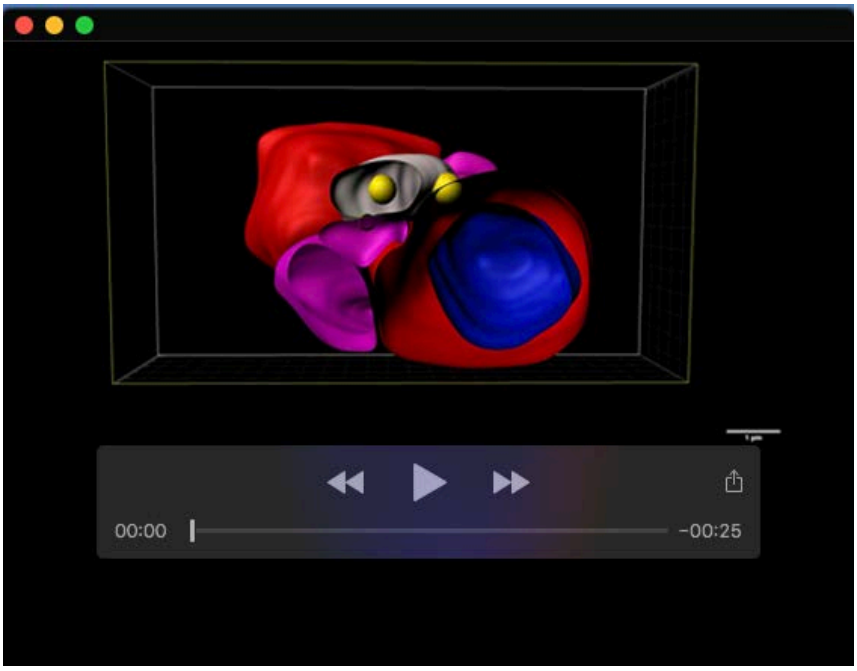

Movie 3. Tridimensional rendering of the primordial germ line displaying the proto-rachis (white compartment), to which both PGCs (red, with nuclei in blue) and membrane lobes (magenta) are connected via intercellular bridges (yellow spheres). This rendering was made from reconstructed EM images. Each image was imported into Inkscape software (v1.1) and the membrane defining each compartment was manually traced. To make intercellular bridges more visible, each was defined as a yellow sphere with a diameter equal to that of the bridge. Each compartment was then filled with colour in separate channels (1 channel per colour) and saved as a tif file. The file was imported into Imaris software (v9.2.1, Bitplane) and the "surface" tool was used to generate a 3D rendering of each defined compartment in each slice. The "clipping plane" tool was used to generate a composite image of each slice and these composite images were assembled with ImageJ software into a movie that sequentially goes from the bottom to the top of the primordial germ line. The "animation" tool from Imaris software was used to rotate the entire reconstructed 3D image.

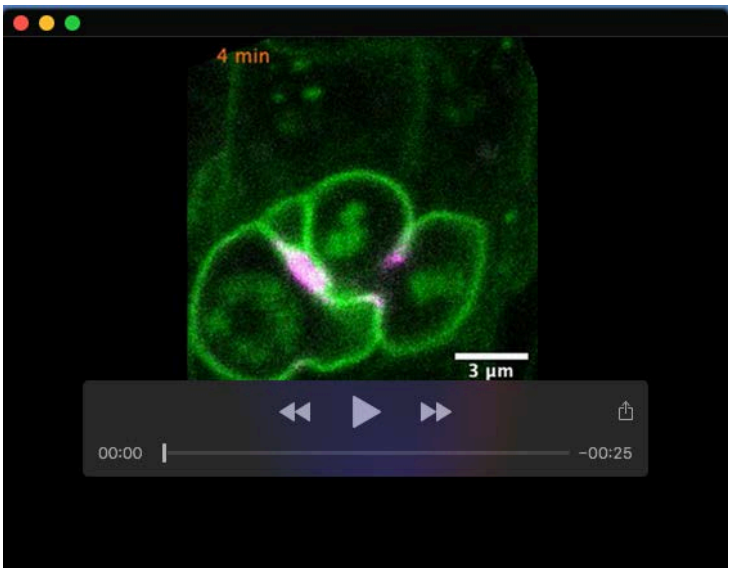

Movie 4. Time-lapse movie of the first division of the PGCs (same images as shown in figure 3C), in animals co-expressing mNG::ANI-1, a membrane (TagRFP::PH) and a histone (mCherry::HIS-58) marker. Images were acquired every 2 min and are played at 3 frames per sec.

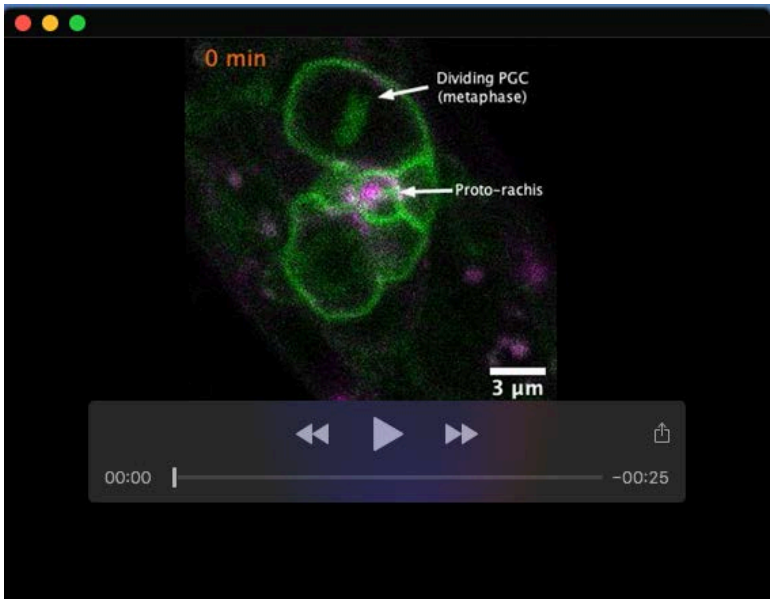

Movie 5. Time-lapse movie of the first division of the PGCs (same images as shown in figure S4A), in animals co-expressing NMY-2::GFP, a membrane (TagRFP::PH) and a histone (mCherry::HIS-58) marker. Images were acquired every 2 min and are played 3 frames per sec.

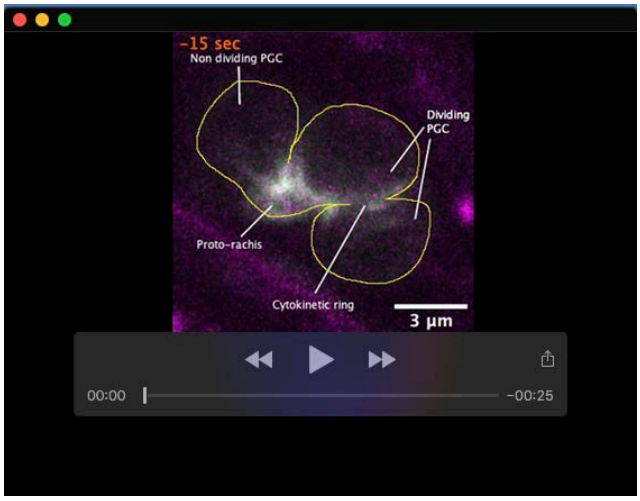

Movie 6. Time-lapse movie of the primordial germ line with one PGC undergoing cytokinesis before and after Dendra2 fluorescence photoconversion (same images as shown in figure 4B), in animals co-expressing mNG::ANI-1 and cytoplasmic Dendra2. Images were acquired every 15 sec and are played at 1 frame per sec.

Supplemental References

1. **Amini, R., Goupil, E., Labella, S., Zetka, M., Maddox, A. S., Labbé, J. C. and Chartier, N. T.** (2014). *C. elegans* Anillin proteins regulate intercellular bridge stability and germline syncytial organization. *J Cell Biol* **206**, 129-143.
2. **Brenner, S.** (1974). The genetics of *Caenorhabditis elegans*. *Genetics* **77**, 71-94.
3. **Chihara, D. and Nance, J.** (2012). An E-cadherin-mediated hitchhiking mechanism for *C. elegans* germ cell internalization during gastrulation. *Development* **139**, 2547-2556.
4. **Dickinson, D. J., Schwager, F., Pintard, L., Gotta, M. and Goldstein, B.** (2017). A Single-Cell Biochemistry Approach Reveals PAR Complex Dynamics during Cell Polarization. *Dev Cell* **42**, 416-434 e411.
5. **Green, R. A., Kao, H. L., Audhya, A., Arur, S., Mayers, J. R., Fridolfsson, H. N., Schulman, M., Schloissnig, S., Niessen, S., Laband, K., et al.** (2011). A high-resolution *C. elegans* essential gene network based on phenotypic profiling of a complex tissue. *Cell* **145**, 470-482.
6. **Griffin, E. E., Odde, D. J. and Seydoux, G.** (2011). Regulation of the MEX-5 gradient by a spatially segregated kinase/phosphatase cycle. *Cell* **146**, 955-968.

7. **Heppert, J. K., Dickinson, D. J., Pani, A. M., Higgins, C. D., Steward, A., Ahringer, J., Kuhn, J. R. and Goldstein, B.** (2016). Comparative assessment of fluorescent proteins for in vivo imaging in an animal model system. *Mol Biol Cell* **27**, 3385-3394.
8. **Kachur, T. M., Audhya, A. and Pilgrim, D. B.** (2008). UNC-45 is required for NMY-2 contractile function in early embryonic polarity establishment and germline cellularization in *C. elegans*. *Dev Biol* **314**, 287-299.
9. **Lee, K. Y., Green, R. A., Gutierrez, E., Gomez-Cavazos, J. S., Kolotuev, I., Wang, S., Desai, A., Groisman, A. and Oegema, K.** (2018). CYK-4 functions independently of its centralspindlin partner ZEN-4 to cellularize oocytes in germline syncytia. *Elife* **7**.
10. **Mangal, S., Sacher, J., Kim, T., Osorio, D. S., Motegi, F., Carvalho, A. X., Oegema, K. and Zanin, E.** (2018). TPXL-1 activates Aurora A to clear contractile ring components from the polar cortex during cytokinesis. *J Cell Biol* **217**, 837-848.
11. **McNally, K., Audhya, A., Oegema, K. and McNally, F. J.** (2006). Katanin controls mitotic and meiotic spindle length. *J Cell Biol* **175**, 881-891.
12. **Nance, J., Munro, E. M. and Priess, J. R.** (2003). *C. elegans* PAR-3 and PAR-6 are required for apicobasal asymmetries associated with cell adhesion and gastrulation. *Development* **130**, 5339-5350.
13. **Rehain-Bell, K., Love, A., Werner, M. E., MacLeod, I., Yates, J. R., 3rd and Maddox, A. S.** (2017). A Sterile 20 Family Kinase and Its Co-factor CCM-3 Regulate Contractile Ring Proteins on Germline Intercellular Bridges. *Curr Biol* **27**, 860-867.
14. **Strome, S., Powers, J., Dunn, M., Reese, K., Malone, C. J., White, J., Seydoux, G. and Saxton, W.** (2001). Spindle dynamics and the role of gamma-tubulin in early *Caenorhabditis elegans* embryos. *Mol Biol Cell* **12**, 1751-1764.